9-10-2021

Investigating Influence of Geometry and Operating Conditions on Local Current, Concentration, and Crossover in Alkaline Water Electrolysis Using Computational Fluid Dynamics

J. S. Lopata

S-G. Kang

H-S. Cho

C-H. Kim

J. W. Weidner

See next page for additional authors

Publication Info

Published in *Electrochimica Acta*, Volume 390, 2021.

Author(s)

J. S. Lopata, S-G. Kang, H-S. Cho, C-H. Kim, J. W. Weidner, and Sirivatch Shimpalee

Electrochimica Acta 390 (2021) 138802

Contents lists available at ScienceDirect

Electrochimica Acta

journal homepage: www.elsevier.com/locate/electacta

Investigating influence of geometry and operating conditions on local current, concentration, and crossover in alkaline water electrolysis using computational fluid dynamics

J.S. Lopata[a], S-G. Kang[b], H-S. Cho[c,*], C-H. Kim[c], J.W. Weidner[d], S. Shimpalee[a,*]

[a] Department of Chemical Engineering, University of South Carolina, Columbia, SC U.S.A.
[b] Gwangju Institute of Science and Technology, Gwangju, South Korea
[c] Korea Institute of Energy Research, Daejeon, South Korea
[d] College of Engineering and Applied Science, University of Cincinnati, Cincinnati, OH U.S.A.

ARTICLE INFO

Article history:
Received 18 May 2021
Revised 11 June 2021
Accepted 15 June 2021
Available online 22 June 2021

Keywords:
Three-dimensional
Pseudo-two-phase
Current distribution
Electrode/separator interface
Capillary action

ABSTRACT

We use a three-dimensional computational fluid dynamics model to examine the liquid saturation, KOH concentration, and gas crossover in an alkaline diaphragm water electrolysis device. The effects of cell potential, solution feed rate, and aspects of the design such as the locations and widths of channels on performance and crossover were studied. The results build a case for implementing a separator transport model and an electrode/separator interface model because of the concentration changes observed at the anode and cathode. Simulations suggest a strong relationship between solution feed rate and the nature of dissolved gas crossover through the diaphragm due to the differential liquid pressure driving force. This work underscores the importance of three-dimensional modeling for the design of electrochemical cells, as it can identify issues linked to the geometry, e.g., low local current density or high local gas crossover.

1. Introduction

1.1. Overview

There is a consensus among a diversity of scientists and most governments that climate change is a major threat to the wellbeing of humanity. In the most recent complete synthesis report from the Intergovernmental Panel on Climate Change (IPCC), as of writing, climate change is directly causing more natural disasters and negatively impacting access to clean water and crop yields [1]. This has been motivating the transformation of the energy and transportation sectors. Hydrogen is expected to play a role as an energy carrier, which would heighten the demand for hydrogen fuel. Preferably, demand should be satisfied using renewable sources of energy such as solar or wind power to generate so-called “green hydrogen” via water electrolysis. However, steam reforming continues to be the least expensive method of producing hydrogen. Electrolysis has advantages in some circumstances, such as when it is more economical to produce hydrogen on-site at a smaller scale than steam reforming. This may perhaps be for transportation or storing grid energy generated from intermittent renewable sources such as wind and solar, the cost of which is trending downward.

Alkaline diaphragm water electrolysis (ADWE) is a widespread, heavily established process. Its high durability [2] and low cost [3] renders it favorable for small- to mid-scale applications, such as grid storage or on-site generation for industrial purposes. Compared with the newly commercialized polymer electrolyte membrane water electrolysis (PEMWE), ADWE is very inexpensive, requiring no precious metals or titanium to withstand a corrosive acidic environment when polarized. Consequently, it depends only on abundant elements such as iron and nickel for electrocatalytic activity [4]. ADWE devices are subject to greater resistance losses than their PEMWE counterparts, which are attributed to the

---

Abbreviations: ADWE, Alkaline diaphragm water electrolysis; CFD, Computational fluid dynamics; CL, Catalyst layer; DLP, Differential liquid pressure; ESI, Electrode/separator interface; HER, Hydrogen evolution reaction; OER, Oxygen evolution reaction; PEMWE, Polymer electrolyte membrane water electrolysis; PTL, Porous transport layer; 3D, Three-dimensional; %LFL, Percent lower flammability limit; $\%H_2P$, Percent hydrogen purity.

* Corresponding authors.
E-mail addresses: hscho@kier.re.kr (H-S. Cho), shimpale@cec.sc.edu (S. Shimpalee).

https://doi.org/10.1016/j.electacta.2021.138802

electrolyte-filled porous diaphragm. However, this is compensated by a relatively high electrocatalytic activity that allows ADWE cell efficiency to rival that of PEMWE within a narrow range of current densities [4].

1.2. Operating principle

ADWE devices split liquid water into hydrogen and oxygen gases using an aqueous, high-pH electrolyte to transport ions through a porous separator. The present state-of-the-art separator most widely used is Zirfon®, which is not ion-selective. In ADWE, the anodic oxygen evolution reaction (OER) and cathodic hydrogen evolution reaction (HER), along with their standard reduction potentials, are:

$$OH^- \rightarrow \tfrac{1}{4}O_2 + \tfrac{1}{2}H_2O + e^- \boldsymbol{E^{\circ}_{eq,a}} = 0.401\ \boldsymbol{V\ vs.\ SHE}\{1\}$$

$$H_2O\ +\ e^-\ \rightarrow\ \tfrac{1}{2}H_2 + OH^- \boldsymbol{E^{\circ}_{eq,c}} = -0.829\ \boldsymbol{V\ vs.\ SHE}\{2\}$$

OH^- migrates from the cathode, where it is produced, to the anode, where it is consumed. Liquid water is consumed at the cathode, but some is generated in the OER. An alkali hydroxide solution, typically NaOH or KOH, is fed to the anode and cathode during operation. The optimal concentration of the solution, largely due to the conductivity, is about 25-30 wt% and depends on temperature [5,6]. The use of an aqueous electrolyte leads to an assortment of challenges. The diaphragm must be porous to accommodate the electrolyte, which contains the OH^- charge carriers, but it must also be selective to the liquid-phase, prohibiting undesired gas crossover. This requires a hydrophilic material with high porosity and a small pore size, Zirfon® being one. Additionally, the presence of the gas phase negatively impacts the kinetic and resistive losses quite strongly because it impedes ion transport to and from reaction surfaces [7] and the diaphragm [8], respectively.

1.3. Current state of research

Experimental studies of ADWE devices have concentrated on improving electrocatalytic activity [9,10], mitigating or preventing gas crossover [11–13], and minimizing kinetic and resistive losses [5,14]. This work addresses voltage losses and crossover by observing the distributions of liquid saturation, solution concentration, and gas crossover predicted by computational fluid dynamics (CFD) analysis. First, we discuss the electrolyte gap between the electrodes and separator, capillary action in porous media, and the mechanisms of gas crossover.

1.4. The electrolyte gap

Conventionally, ADWE cells are built with a gap between the electrodes and separator because until recently, electrodes were typically solid metal plates and an escape channel was required for evolved gases to be expelled. This came at a disadvantage, namely the potential losses attributed to the decrease in effective conductivity of the solution within the gap. These losses are dependent on the gap width and the rate of gas production. One early research effort sought to optimize the gap width in conventional ADWE, concluding that a 2 mm gap width between the electrode and separator led to the best performance [15].

Porous electrodes and developments in diaphragm materials allowed cells to be assembled with a zero-gap configuration because bubbles can escape through the pores of the electrode and crossover is effectively limited by today's diaphragms [16]. Zirfon®, being 85% ZrO_2 and 15% polysulfone, is hydrophilic, unlike the traditional porous polymer diaphragms. The resulting high bubble point allows Zirfon® to effectively separate product gases at atmospheric pressure.

While the zero-gap configuration offers the advantage of lower resistance, the cell resistance still exceeds open-circuit zero-gap measurements of diaphragm resistance [17] and calculated values based on the properties of the solution and separator, namely porosity, tortuosity, and electrolyte resistivity [8,18]. The presence of the gas phase at the electrode/separator interface (ESI) is the most likely cause, in light of experimental work conducted by Kienzlen et al. [19] using perforated plate electrodes. Their work showed that optimal performance is achieved with a gap width similar in magnitude to the electrode pore size to allow gas bubbles to escape. In our recent experimental work on PEMWE devices [20], we showed that the gas phase occupies more of the region between the porous transport layer (PTL) and separator when the catalyst layer (CL) is very thin, i.e., the PTL is much closer to the membrane. These results suggest that there is an interfacial resistance that contributes to the measured cell resistance.

1.5. Capillary action in electrolysis devices

Porous media facilitate the ease of two-phase flow in electrolysis devices by providing pathways for liquid flowing toward and gas flowing away from reaction sites. The coexistence of the gas and liquid phases bears with it capillary action due to forces at the boundaries between the fluid, gas, and solid phases. The dimensionless quantity defined by Leverett [21] has been empirically fitted for other systems, including fuel cells and electrolyzers [22–24]. The Leverett function used by Wang et al. [25] is widely used. Kumbur et al. [24] compiled some well-known relative permeability models, used in conjunction with the Leverett function, from literature. To incorporate capillary action into a pseudo-two-phase model, in which there is only one governing equation each for mass and momentum conservation, we can specify an effective capillary diffusivity [26,27].

Liquid saturation and concentration distributions depend on the capillary model. Liquid saturation determines the fraction of the catalyst surface that is utilized, and concentration affects the cell resistance. The difference in liquid saturation across the separator can also drive the through-plane flow of solution if the total pressures at the anode and cathode are balanced because there would be a difference in liquid pressures in this scenario. As we cover in the next section, this can have an effect on gas crossover.

1.6. Crossover

Schalenbach et al. [28] discussed three components of the crossover mechanism in alkaline water electrolysis – diffusion of dissolved gases, convection of fluid containing dissolved gases, and gas bubbling – and quantified the effective hydrogen permeability through a Zirfon® separator immersed in KOH solution. In this work, we use their findings to model the local crossover of hydrogen and oxygen through the separator. If we neglect gas bubbling through the separator, which occurs when the differential gas pressure exceeds the bubble point of the separator, gas crossover is assumed to be entirely dependent on the flow rate of the solution through the separator. This depends primarily on two driving forces: differential liquid pressure (DLP) across the separator and electroosmotic drag due to the migration of OH^-. Differential liquid pressure is influenced by pressure drops from inlets to outlets and capillary action. This can drive fluid flow in either direction depending on operating conditions, especially the feed rates. Solution will tend to pass from the porous electrode into the separator near the inlets, where liquid pressure is generally high. Solution should also move from high to low liquid saturation if capillary action is the dominant factor of DLP. Haverkort [18] observed the flow of water from anode to cathode in experiments, which agreed with expectations based on an ion transport model [18,29].

We expect that DLP-driven fluid flow also may explain this flow if the liquid pressure is higher at the anode than at the cathode. While pressure gradients within the separator were considered in that model, it was assumed that no DLP was present across the separator.

Electroosmotic drag, which acts on water from cathode to anode, may also be an important factor to consider, possibly limiting the flow rate of water from anode to cathode (or conversely enhancing the flow rate of water from cathode to anode) and leading to more hydrogen crossover. Haverkort [18] suggests an electroosmotic drag coefficient of 6 ± 1 mol H_2O (mol OH^-)$^{-1}$ while Trinke et al. [11] suggests a value of 1.3 based on anion exchange membrane characterization [30]. This disagreement highlights the need to characterize electroosmotic drag in Zirfon®.

1.7. Objectives

Two-phase flow simulations applied to electrolysis date back to 2D CFD modeling work by Mat et al. [31], who developed a mathematical model predicting void fraction distributions in conventional ADWE cell channels. The experimental work of Reigel et al. [32] validated their solutions. This work demonstrated the importance of understanding two-phase flow by showing quantitative effects of hydrogen bubbles on the electrochemically active area and the effective conductivity of the solution. Since then, two-phase flow models for electrolysis cells have been presented by many authors [33–39], who focused on computing validated flow and liquid saturation distributions without predicting nonuniformity in the electrochemical reaction. Recently, Rodríguez and Amores [40] released a computational study of the effects of the gas phase on cell performance. They expanded upon the previous study by Mat et al. [31] using a 2D CFD model to study the performance of a full conventional ADWE cell, including the effects of temperature, solution conductivity, and gap width on performance.

This work aims to apply 3D CFD to the present generation of zero-gap ADWE devices. Herein, we use computed distributions of current density, liquid saturation, solution concentration, and gas crossover to identify needs for further research to address. Specifically, we bring to light the effects of geometry on local variables, the intricate nature of gas crossover, and whether additional models of ion transport in the separator and bubble coverage at the ESI are necessary for future work.

2. Methodology

2.1. Experimental procedure

As shown in Fig. 1a, a single cell with an active area of approximately 36 cm^2 was constructed in a zero-gap configuration with nickel PTLs, nickel current collectors, and a Zirfon PERL UTP-500 separator. Raney nickel and nickel-iron layered double hydroxide (LDH) were used as the cathodic and anodic catalysts, respectively, both on nickel foam supports. Nickel foams were also used as PTLs. The current collectors contained no flow fields, instead directing the feed solution into the porous media. Cell performance was evaluated at a temperature of 80°C and a feed rate of 30 wt% KOH solution equal to 400 mL min^{-1} – i.e., ~11.1 mL min^{-1} cm^{-2} – into each half cell. The anolyte and catholyte were fed in a counter-current configuration. Galvanostatic polarization experiments were conducted by incrementing current density in the range from 0 to 2 A cm^{-2} using a Biologic HCP-803 potentiostat/galvanostat. Each current was applied for at least 10 min to obtain a steady-state result. The electrolyzer was operated in a partially separated cycle, which allowed partial mixing of the catholyte and anolyte by opening a mixing pipe valve between the KOH chambers to control the OH^- concentration. A schematic of the overall process is illustrated in Fig. 1b.

2.2. Model geometry

The single cell geometry, shown in Fig. 2, consisted of two plates, manifolds with extrusions at the inlets and outlets (extrusions not shown), two PTLs, two electrodes, and a diaphragm separator. The computational domain was based on a design concept, with the component thicknesses and general assembly configuration based on the experimental cell. Table 1 lists all regions and their interfaces, assigning unique superscripts to each region, grouping of regions, and interfaces for use in symbolic equations. The cross-sectional area of the cell was about 729 cm^2 and the electrodes, PTLs, and separator were 0.7, 0.9, and 0.46 mm, respectively. A thin mesher was used to achieve accurate and efficient discretization of this thin domain. The thin meshing technique allowed for a high-quality representation of the geometry with a total of 477,559 cells. Through early testing with a simple rectangular geometry, it was found that fluid flow velocity through a thin region bound by walls with no-slip conditions was accurately computed when at least 8 thin layers (368 cells) were generated in the mesh. Doubling the number of thin layers to 16 (736 cells) resulted in a 3.3% increase in the maximum velocity while halving the thin layers (184 cells) led to a 12% decrease in maximum velocity. Therefore, the electrodes and PTLs were each given 4 thin layers for a total of 8 layers between the plate and the separator on both sides of the cell. The manifolds were meshed with only 4 layers in thin sections, which provided an acceptable flow computation for these regions, which were not in close proximity to the vast majority of the electrochemically active surface. The 1.6 mm manifolds injected solution directly into the electrodes and PTLs by design, as opposed to having non-porous flow channels between the PTL and plate, similarly to the experimental cell.

The mesh size at the injection/ejection areas in the electrodes and PTLs was set to a small value of 0.6 mm near the manifolds and allowed to expand to a maximum of 6.7 mm toward the middle of the flow field. This was in expectation of the gradients that would form in proximity of the injection/ejection areas. A large target mesh size was applied to the plates, in which only potential and energy are modeled. However, due to the thinness of the plates in some sections, compatibility refinement was enabled to ensure high cell quality in sections of the plate near the internal porous media. Fig. 2c exhibits the outcome of this refinement.

By changing the number of thin layers in each region, coarse and fine meshes were produced, the total number of cells being 323,329 and 825,080, respectively. At 2.4V, the simulated average current density varied by about 2% among meshes.

2.3. Governing equations

In this section, average properties are accented according to their weighting; $\bar{\varphi}$, $\hat{\varphi}$, and $\breve{\varphi}$ are respectively the volume-weighted, mass-weighted, and quantity-weighted averages of the hypothetical property φ. Furthermore, superficial properties, with the exception of velocity and ionic diffusivity, are defined as $\varphi^S = s\varphi$, s being liquid saturation. The parameter values and relationships not included in the text are provided in Tables 2 and 3.

We employed the pseudo-two-phase flow assumption to model flow within the cell. It was assumed that the gas and liquid phases traveled at the same advective velocity $\overset{\frown}{\underline{v}}^{S} = \epsilon \hat{\underline{v}}$, with ϵ being porosity, at every point in the domain. This reduced the number of governing equations to one equation each for mass and momentum conservation,

$$\nabla \cdot \left(\bar{\rho} \hat{\underline{v}}^S \right) = \sum_i S_{i=w,wv} = 0 \quad (1)$$

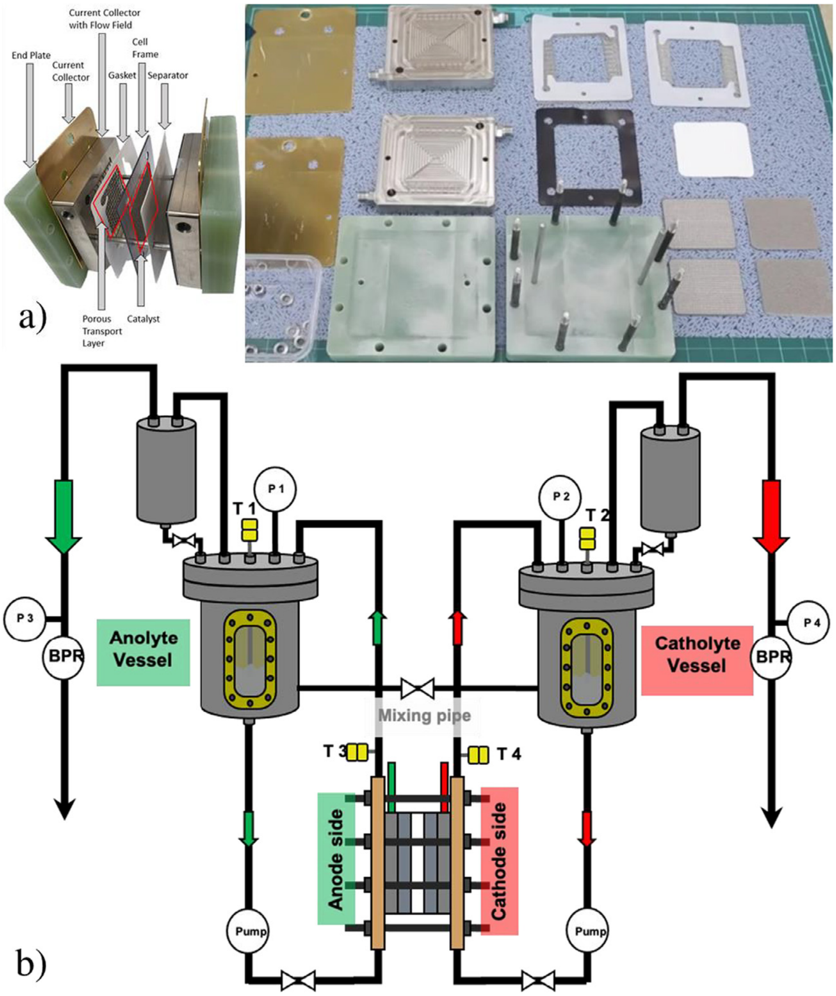

Fig. 1. a) Schematic of the experimental test station. b) Cell assembly and components.

Table 1
Model Geometry – Regions, Interfaces, and Designated Superscripts

Region	Superscript or Label	Has Interface With:
Anode	{a}	{sep, ptla, cca, ima, oma}
Cathode	{c}	{sep, ptlc, ccc, imc, omc}
Separator	{sep}	{a, c}
Anode PTL	{ptla}	{a, cca, ima, oma}
Cathode PTL	{ptlc}	{c, ccc, imc, omc}
[a, c, ptla, ptlc}	{por}	All
Anode Current Collector	{cca}	{a, ptla, ima, oma, ∞}, + terminal
Cathode Current Collector	{ccc}	{c, ptlc, imc, omc, ∞}, - terminal
Anode Inlet Manifold	{ima}	{a, ptla, cca}, anode inlet
Anode Outlet Manifold	{oma}	{a, ptla, cca}, anode outlet
Cathode Inlet Manifold	{imc}	{c, ptlc, ccc}, cathode inlet
Cathode Outlet Manifold	{omc}	{c, ptlc, ccc}, cathode outlet
All Fluid Regions	{f}	All
All Manifolds	{man}	all except separator
Environment	{∞}	{cca, ccc}

Interface	Superscript	Interface	Superscript
{a}/{sep}	{a}	{imc}/cathode inlet	{inc}
{c}/{sep}	{c}	{oma}/anode outlet	{outa}
{cca}/{ima}, {cca}/{oma}	{ccma}	{omc}/cathode outlet	{outc}
{ccc}/{imc}, {ccc}/{omc}	{ccmc}	{ina, inc, outa, outc}	{io}
{cca}/{∞}, {ccc}/{∞}	{cc∞}	{cca}/+ terminal	{+}
{ima}/anode inlet	{ina}	{ccc}/- terminal	{-}

Table 2
Parameters

Latin

Param.	Value	Unit	Ref.
$D^{ref}_{H_2-O_2}$	4.17e-05	m^2 s^{-1}	[42]
$D^{ref}_{H_2-wv}$	1.012e-04	m^2 s^{-1}	[42]
$D^{ref}_{O_2-wv}$	2.82e-05	m^2 s^{-1}	[42]
E_{cell}	{1.6, 1.8, 2.0, 2.2, 2.4}	V	
$E^{\circ}_{eq,a}$	1.2288	V vs. $E^{\circ}_{eq,c}$	
$E^{\circ}_{eq,c}$	0	V vs. $E^{\circ}_{eq,c}$	
$E_{tn,a}$	1.73	V vs. $E^{\circ}_{eq,c}$	
$E_{tn,c}$	0.25	V vs. $E^{\circ}_{eq,c}$	
F	96,485,333	C kmol^{-1}	
$L^{\{sep\}}$	4.6e-04	m	
M_{H_2}	2.016	kg kmol^{-1}	
M_{O_2}	31.999	kg kmol^{-1}	
M_{OH^-}	17.007	kg kmol^{-1}	
M_w	18.015	kg kmol^{-1}	
N_{Sc}	100	none	
$P^{ref}_{H_2-O_2}$	101325	Pa	[42]
$P^{ref}_{H_2-wv}$	101325	Pa	[42]
$P^{ref}_{O_2-wv}$	101325	Pa	[42]
Q	{8.107, 2.027}	L min^{-1}	
$\mathcal{R}$	8314.66	J kmol^{-1} K^{-1}	
R_{esi}	1.35e-05	Ω m^2	
$T^{\{ina,inc\}}$	353.15	K	
$T^{\{\infty\}}$	312.15	K	
$T^{ref}_{H_2}$	293.85	K	[47,48]
$T^{ref}_{O_2}$	292.25	K	[47,48]
$T^{ref}_{H_2-O_2}$	308.05	K	[42]
$T^{ref}_{H_2-wv}$	308.05	K	[42]
$T^{ref}_{O_2-wv}$	322.65	K	[42]
U	100	W m^{-2} K^{-1}	
b	1.5	none	
$b^{\{sep\}}$	2.3	none	[17]
$c_P^{\{sep\}}$	2120	J kg^{-1} K^{-1}	
c_{P,H_2}	14315.8	J kg^{-1} K^{-1}	[49]
c_{P,O_2}	920.425	J kg^{-1} K^{-1}	[49]
$c_{P,L}$	2979	J kg^{-1} K^{-1}	[50,51]
$c_{P,wv}$	1938.19	J kg^{-1} K^{-1}	[49]
$i^{ref}_{0,a}$	1.28	A m^{-2}	[52]
$i^{ref}_{0,c}$	7.54	A m^{-2}	[9]
k_B	1.38065e-23	J K^{-1}	

Greek

Parameter	Value	Unit	
α_a	1.52	none	[52]
α_c	1.178	none	[53]
$\epsilon^{\{a,c\}}$	0.76	none	
$\epsilon^{\{ptla,ptlc\}}$	0.67	none	
$\epsilon^{\{sep\}}$	0.576	none	[12]
θ	0.52	rad	
$\kappa^{\{por\}}$	1.0e-08	m^2	
$\kappa^{\{sep\}}$	7.0e-16	m^2	[28]
λ_{Ni}	90	W m^{-1} K^{-1}	
$\lambda^{\{sep\}}$	1	W m^{-1} K^{-1}	
λ_w	0.65	W m^{-1} K^{-1}	
$\mu^{ref}_{H_2}$	8.76e-06	Pa s	[47,48]
$\mu^{ref}_{O_2}$	2.018e-05	Pa s	[47,48]
ν_{H_2}	0.5	mol (mol e$^-$)$^{-1}$	
ν_{O_2}	0.25	mol (mol e$^-$)$^{-1}$	
$\nu_{OH^-,a}$	-1	mol (mol e$^-$)$^{-1}$	
$\nu_{OH^-,c}$	1	mol (mol e$^-$)$^{-1}$	
$\nu_{w,a}$	0.5	mol (mol e$^-$)$^{-1}$	
$\nu_{w,c}$	-1	mol (mol e$^-$)$^{-1}$	

K_1-K_{73}

Param.	Value	Unit	Ref.
K_1	1.89745	m^2 s^{-1}	
K_2	-8.53249	None	
K_3	0.329562	m^2 s^{-1}	
K_4	0.410319	10^{20} J	
K_5	-4.15603	None	
K_6	3.17473	10^{20} J	
K_7	0.0475058	kmol m^{-3} Pa^{-1}	
K_8	-18.6545	None	
K_9	1.06025	None	
K_{10}	1.98037	10^{20} J	
K_{11}	4.44386	10^{20} J	
K_{12}	-2295.71	K	
K_{13}	0.00770824	m^6 kmol^{-2}	
K_{14}	-0.240895	m^3 kmol^{-1}	
K_{15}	8.37624	None	
K_{16}	1.9746e10	K$^{-K\_17}$	
K_{17}	-5.33093	None	
K_{18}	8.91459e-04	K^{-1}	
K_{19}	-0.447179	None	
K_{20}	-3.498	None	[46]
K_{21}	37.93	None	[46]
K_{22}	-6426.32	K	[46]
K_{23}	0.016214	None	[46]
K_{24}	-0.13802	m^3 kmol^{-1}	[46]
K_{25}	0.1933	m$^{1.5}$ kmol$^{-0.5}$	[46]
K_{26}	1.28756e-09	mol kg^{-1} m^9 kmol^{-3} K^{-2}	
K_{27}	4.57346e-07	mol kg^{-1} m^9 kmol^{-3} K^{-1}	
K_{28}	8.51811e-04	mol kg^{-1} m^9 kmol^{-3}	
K_{29}	-1.87305e-08	mol kg^{-1} m^6 kmol^{-2} K^{-2}	
K_{30}	3.52482e-06	mol kg^{-1} m^6 kmol^{-2} K^{-1}	
K_{31}	0.00764237	mol kg^{-1} m^6 kmol^{-2}	
K_{32}	3.09226e-07	mol kg^{-1} m^3 kmol^{-1} K^{-2}	
K_{33}	3.67376e-04	mol kg^{-1} m^3 kmol^{-1} K^{-1}	
K_{34}	0.869801	mol kg^{-1} m^3 kmol^{-1}	
K_{35}	-0.0151895	None	
K_{36}	-46.8743	None	
K_{37}	343.766	None	
K_{38}	-566.491	None	
K_{39}	472.221	None	
K_{40}	4.34773e-05	K^{-1}	
K_{41}	0.258126	K^{-1}	
K_{42}	-1.38799	K^{-1}	
K_{43}	1.89206	K^{-1}	
K_{44}	-1.39535	K^{-1}	
K_{45}	-1.10721e-07	K^{-2}	
K_{46}	-4.37513e-04	K^{-2}	
K_{47}	0.00228340	K^{-2}	
K_{48}	-0.00398424	K^{-2}	
K_{49}	0.00344981	K^{-2}	
K_{50}	-9.6278e-05	m^6 kmol^{-2} K^{-1}	
K_{51}	0.0324536	m^6 kmol^{-2}	
K_{52}	8.00428e-04	m^3 kmol^{-1} K^{-1}	
K_{53}	-0.138153	m^3 kmol^{-1}	
K_{54}	6.28356e-05	K^{-2}	
K_{55}	-0.0574972	K^{-1}	
K_{56}	11.4473	None	
K_{57}	999.65	kg m^{-3}	[54]
K_{58}	0.20438	kg m^{-3}$^{\circ}$C^{-1}	[54]
K_{59}	-0.06174	kg m^{-3}$^{\circ}$C$^{-1.5}$	[54]
K_{60}	54.59	kg kmol^{-1}	[54]
K_{61}	-0.1156	kg kmol^{-1}$^{\circ}$C^{-1}	[54]
K_{62}	0.001009	kg kmol^{-1}$^{\circ}$C^{-2}	[54]
K_{63}	-4.383	kg m$^{1.5}$ kmol$^{-1.5}$	[54]
K_{64}	0.02343	kg m$^{1.5}$ kmol$^{-1.5}$$^{\circ}$C^{-1}	[54]
K_{65}	-1.865e-4	kg m$^{1.5}$ kmol$^{-1.5}$$^{\circ}$C^{-2}	[54]
K_{66}	-0.342001	S m^{-1} K^{-1}	[6]
K_{67}	0.00119700	S m^{-1} K^{-2}	[6]
K_{68}	-117.298	S m^2 kmol^{-1}	[6]
K_{69}	-0.516794	S m^5 kmol^{-2}	[6]
K_{70}	0.328293	S m^5 kmol^{-2} K^{-1}	[6]
K_{71}	1.19605e04	S m^5 kmol^{-2} K	[6]
K_{72}	0.0624312	S m^8 kmol^{-3}	[6]
K_{73}	-1.8832e-05	S m^5 kmol^{-2} K^{-2}	[6]

Table 3
Material Property Relationships

Equation	Ref.
$J\{s\} = 1.417(1-s) - 2.12(1-s)^2 + 1.263(1-s)^3$	[25,27,41]
$P_{sat} = 101325 * T^{K_{20}} \exp\{K_{21} + \frac{K_{22}}{T}\} * \exp\{K_{23} + K_{24}C_{KOH} + K_{25}\sqrt{C_{KOH}}\}$	[46]
$P^*_{sat} = 101325 * T^{K_{20}} \exp\{K_{21} + \frac{K_{22}}{T}\} * \exp\{K_{23}\}$	[46] (modified)
$m_{KOH} = (K_{26}T^2 + K_{27}T + K_{28}) * C^3_{KOH} + (K_{29}T^2 + K_{30}T + K_{31}) * C^2_{KOH} + (K_{32}T^2 + K_{33}T + K_{34}) * C_{KOH}$	[46] (fitted to within 0.5% error)
$s = \frac{w^S_L}{\rho_L}\left(\sum_i \frac{w^S_i}{\rho_i}\right)^{-1}$	
$w_i = w^S_i\left(\sum_i^{n\in\Pi} w^S_i\right)^{-1}$	
$w_{KOH} = \frac{0.056106 * m_{KOH}}{1 + 0.056106 * m_{KOH}}$	
$w_{wv,sat} = \frac{P_{wv,sat}M_w}{P_{wv,sat}M_w + (P - P_{wv,sat})(y_{O_2}M_{O_2} + y_{H_2}M_{H_2})}$	
$x_{KOH} = \frac{2 * m_{KOH}}{55.5093 + 2 * m_{KOH}}$	[55]
$y_i = y^S_i(\sum_i^{n\in\Pi} y^S_i)^{-1}$	
$\mathrm{Y}_{\pm,m} = \exp\{K_{35} + K_{36}x_{KOH} + K_{37}x^2_{KOH} + K_{38}x^3_{KOH} + K_{39}x^4_{KOH} + (K_{40} + K_{41}x_{KOH} + K_{42}x^2_{KOH} + K_{43}x^3_{KOH} + K_{44}x^4_{KOH}) * T + (K_{45} + K_{46}x_{KOH} + K_{47}x^2_{KOH} + K_{48}x^3_{KOH} + K_{49}x^4_{KOH}) * T^2\}/(1 + 0.03603 * m_{KOH})$	[55] (fitted to within 6% error)
$\gamma_L = 7.25394 \times 10^{-5} * \rho_L - 9.93253 \times 10^{-4}$	[56] (fitted to within 0.9% error, $R^2 = 0.998$)
$\lambda_{eff} = \epsilon \sum_i w^S_i\lambda_i + (1-\epsilon)\lambda_{Ti}$	
$\lambda_{H_2} = 44.79 + 0.4586 * T$	[57]
$\lambda_{O_2} = 3.36 + 0.0759 * T$	[57]
$\lambda_{wv} = 7.23333 + 0.085 * T$	[57]
$\mu_G = y_{H_2}\mu_{H_2} + y_{O_2}\mu_{O_2} + y_{wv}\mu_{wv}$	
$\mu_{H_2} = \mu^{ref}_{H_2}\frac{T^{ref}_{H_2} + 72}{T + 72}(\frac{T}{T^{ref}_{H_2}})^{1.5}$	[47,48]
$\mu_L = 10^{-3} * \exp\{(K_{50}T + K_{51})C^2_{KOH} + (K_{52}T + K_{53})C_{KOH} + K_{54}T^2 + K_{55}T + K_{56}\}$	[51] (fitted to within 7% error)
$\mu_{O_2} = \mu^{ref}_{O_2}\frac{T^{ref}_{O_2} + 127}{T + 127}(\frac{T}{T^{ref}_{O_2}})^{1.5}$	[47,48]
$\mu_{wv} = -3.79625 \times 10^{-17} * P^2 + 1.7407 \times 10^{-11} * P + 1.08872 \times 10^{-5}$	[58] (fitted to within 0.1% error)
$\rho_{i=\{H_2,O_2\}} = PM_i/RT$	
$\rho_L = K_{57} + K_{58}(T - 273.15) + K_{59}(T - 273.15)^{1.5} + K_{60}C_{KOH} + K_{61}C_{KOH}(T - 273.15) + K_{62}C_{KOH}(T - 273.15)^2 + K_{63}C^{1.5}_{KOH} + K_{64}C^{1.5}_{KOH}(T - 273.15) + K_{65}C^{1.5}_{KOH}(T - 273.15)^2$	[54]
$\rho_{wv} = 5.51107 \times 10^{-6} * P + 0.037808$	[58] (fitted to within 0.3% error)
$\sigma = K_{66}T + K_{67}T^2 + K_{68}C_{KOH} + K_{69}C^2_{KOH} + K_{70}TC^2_{KOH} + \frac{K_{71}C^2_{KOH}}{T} + K_{72}C^3_{KOH} + K_{73}(TC_{KOH})^2$	[6]

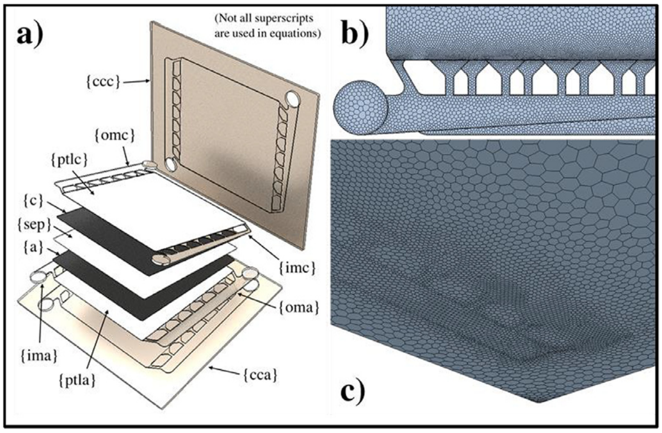

Fig. 2. a) Components of the single cell model, including current collectors, PTLs, electrodes, inlet/outlet manifolds, and the separator. b) A zoomed depiction of the volume mesh of fluid regions near the manifolds. c) The impact of compatibility refinement on the backside of a current collector.

$$\nabla \cdot \left(\bar{\rho}\left(\underline{\hat{v}}^S \otimes \underline{\hat{v}}^S\right)\right) = -\nabla\left(P - \left[1 + \frac{(1-s)^3\mu_L\breve{\rho}_G}{s^3\breve{\mu}_G\rho_L}\right]^{-1} P^{\{por\}}_{cap}\right)\underline{\underline{I}} + \nabla \cdot \underline{\underline{T}} - \left(\underline{\underline{R}}\underline{\hat{v}}^S\right)^{\{por\}} + \underline{\hat{v}}^S \sum_i S_{i=w,wv} \quad (2)$$

in which the terms containing the sum of phase change sources and sinks $\sum_i S_{i=w,wv}$ are equal to zero by nature of mass conservation. $\bar{\rho}$ denotes the volume-weighted average density of the continuum, defined as $s\rho_L + (1-s)\breve{\rho}_G$, with s being the liquid volume fraction, or liquid saturation. The use of quantity-weighted averages $\breve{\rho}_G$ and $\breve{\mu}_G$ is an approximation that lessens operations and has little to no effect on the solution. In Eq. 2, the scalar variables P and μ represent pressure and dynamic viscosity, respectively, while the tensor quantities $\underline{\underline{I}}$, $\underline{\underline{T}}$, and $\underline{\underline{R}}$ are the identity matrix, stress tensor, and viscous resistance tensor, respectively. The factor preceding the capillary pressure $P^{\{por\}}_{cap}$ was derived from Eqs. 3-5, 12, and 16 in Wang and Beckermann [26]. $P_{cap}^{\{por\}}$ was a function of the surface tension γ, contact angle θ, permeability κ, ϵ, and s using the Leverett function $J\{s\}$ [25,27,41].

$$P_{cap}^{\{por\}} = \gamma \cos\{\theta\}\sqrt{\epsilon/\kappa}\ J\{s\} \tag{3}$$

$J\{s\}$ is provided in Table 3. $\underline{\underline{R}}$ was defined as a sum of parallel resistances [26], with the relative permeability of the liquid and gas phases set to s^3 and $(1-s)^3$, respectively:

$$\underline{\underline{R}} = \frac{1}{\kappa}\left[\frac{s^3}{\mu_L} + \frac{(1-s)^3}{\breve{\mu}_G}\right]^{-1}\underline{\underline{I}} \tag{4}$$

The feed velocity was specified at the anode and cathode inlets based on the volumetric flow rate Q and the cross-sectional area $A^{\{ina,inc\}} = 9.08\ \mathrm{cm}^2$ while pressure was specified at the outlets:

$$\left[\bar{\rho}\left(\underline{\hat{v}}^S \cdot \underline{\xi}^{\{ima,imc\}}\right)\right]^{\{ina,inc\}} = \rho_L\left(10^{-3}\left[\frac{m^3}{L}\right] * \frac{1}{60}\left[\frac{\min}{s}\right] * \frac{Q\left[\frac{L}{\min}\right]}{A^{\{ina,inc\}}[m^2]}\right) \tag{5}$$

$$P^{\{outa,outc\}} = 101,325\ Pa \tag{6}$$

Laminar flow was assumed in this model, which was applicable to flow within the porous media. Because turbulence can still exist in the inlet and outlet manifolds, the laminar flow assumption may lead to lower computed pressure drops from inlet to outlet and possibly some degree of deviation from the actual flow distribution. This is mentioned again where applicable, and turbulence will be considered in further studies to understand its effect on performance.

Species conservation is given in Eq. 7,

$$\nabla \cdot \left(\bar{\rho} w_i^S \underline{\hat{v}}\right) = -\int^{\{por\}^b} \nabla \cdot \left(\bar{\rho} D_{i-j} \nabla w_i^S\right) + S_{i=w,wv} \tag{7}$$

in which w_i^S is the superficial mass fraction of species i, b is the Bruggeman exponent, and D_{i-j} is the binary diffusivity of i in j. The left-hand side of Eq. 7 is the convective term and the first term on the right-hand side represents the divergence of diffusive flux relative to the mass-average superficial velocity. S_{wv} is the water evaporation rate, which is given by:

$$S_{wv} = -S_w = \min\left\{s\rho_L,\ (1-s)\breve{\rho}_G(w_{wv,sat} - w_{wv})\right\} \tag{8}$$

The mass fraction of the liquid phase was set to 1 at the inlets and, in case of any reverse flow, the outlets. At the electrodes, boundary normal species fluxes n_i were specified for the electrochemical reaction in Eq. 9 and crossover in Eqs. 10 and 11, with positive values denoting local generation and negative values denoting local consumption:

$$n_i^{rxn} = \nu_i M_i/F * \left(\underline{i} \cdot \underline{\xi}^{\{sep,c\}}\right)^{\{a,c\}} \tag{9}$$

$$n_{i=H_2,O_2}^{co,\{a,c\}} = \{+,-\}C_{i,sat}^{\{c,a\}} M_i\left[\frac{\int^{\{sep\}}}{\tau^{\{sep\}}} D_{i-KOH}\frac{\Delta P_i}{L^{\{sep\}}} + P_{H_2,O_2}^{\{c,a\}}\left(\frac{\kappa^{\{sep\}}\Delta(P-P_{cap})}{\mu_L L^{\{sep\}}} + \frac{n_d M_w}{\rho_L F}\left(\underline{i} \cdot \underline{\xi}^{\{sep,c\}}\right)^{\{a,c\}}\right)\right] \tag{10}$$

$$n_w^{co,\{a,c\}} = \{+,-\}\frac{\kappa^{\{sep\}}\rho_L\Delta(P-P_{cap})}{\mu_L L^{\{sep\}}} + \frac{n_d M_w}{F}\left(\underline{i} \cdot \underline{\xi}^{\{sep,c\}}\right)^{\{a,c\}} \tag{11}$$

In Eq. 9, ν_i is the stoichiometric coefficient of i, normalized such that $\nu_{e^-} = 1$. M_i is molecular mass, F is Faraday's constant, and $(\underline{\boldsymbol{i}} \cdot \underline{\boldsymbol{\xi}}^{\{sep,c\}})^{\{a,c\}}$ is the through-plane component of the current density at either the anode or cathode. Eq. 10 applied the methodology and findings from Schalenbach et al. [28] to calculate the mass fluxes of hydrogen and oxygen across the separator. Here, $\tau^{\{sep\}}$ and $L^{\{sep\}}$ are the tortuosity and thickness of the separator, respectively, and $C_{i,sat}$ is the solubility of i. The difference in the bracketed expressions on the right-hand sides of Eqs. 10 and 11 across the separator determined the fluxes of species due to diffusion and convection. The $\{+,\ -\}$ indicates the sign of the first term on the right-hand sides of these equations at the corresponding electrode. These terms are positive at the anode and negative at the cathode. The terms containing the electroosmotic drag coefficient n_d represented fluxes due to electroosmotic drag. Bubbling was neglected, so water vapor flux was neglected because this assumption required water to be in the liquid phase in order to cross over.

The conservation of charge was applied to all regions, with σ being the conductivity and E the potential,

$$\nabla \cdot \underline{i} = -(1-\int)^{\{por\}^b}\ \nabla \cdot (\sigma \nabla E) = 0 \tag{12}$$

and the following boundary conditions were set at the terminals in Eq. 13, anode interface in Eq. 14, and cathode interface in Eq. 15:

$$\left[E^{\{+\}}, E^{\{-\}}\right] = [E_{cell}, 0] \tag{13}$$

$$\left(\underline{i} \cdot \underline{\xi}^{\{sep\}}\right)^{\{a\}} = \left(E_-^{\{a\}} - E_+^{\{a\}}\right)/R_{tk}^{\{a\}} \tag{14}$$

$$\left(\underline{i} \cdot \underline{\xi}^{\{c\}}\right)^{\{c\}} = \left(E_-^{\{c\}} - E_+^{\{c\}}\right)/R_{tk}^{\{c\}} \tag{15}$$

The area-specific thermodynamic and kinetic resistance at the electrode interfaces, $R_{tk}^{\{a,c\}}$, is determined using a stabilization procedure that reinforces Eq. 12 when used in conjunction with the built-in potential solver. This will be described in "Electrochemical Reaction Equations." To prevent potential solver divergence, we used an additional boundary condition to insulate the manifold walls from the current collectors:

$$R_\Omega^{\{ccma,ccmc\}} = 10^{20} \tag{16}$$

Eq. 17, which includes terms for conduction in all regions, convection, and viscous stress heating in fluid regions, ohmic heating in the separator, and evaporative cooling in porous media, was applied to the entire domain with applicable terms and factors for each region,

$$\nabla \cdot \left(\bar{\rho}\hat{h}\underline{\hat{v}}^S\right)^{\{f\}} = -\nabla \cdot \left(\lambda_{eff}\nabla T\right) + \nabla \cdot \left(\underline{\underline{T}} \cdot \underline{\widehat{v}}^S\right)^{\{f\}} + (\underline{i} \cdot \nabla E)^{\{sep\}} - h_w^{vap} S_{wv} \tag{17}$$

in which h was the specific enthalpy and λ_{eff} was the effective thermal conductivity of the region. Heat fluxes were specified at inlets, outlets, electrode boundaries, and outer surfaces of the plates:

$$\left(\underline{q} \cdot \underline{\xi}^{\{man\}}\right)^{\{io\}} = \left(\bar{\rho}\hat{h}\left(\underline{\hat{v}}^S \cdot \underline{\xi}^{\{man\}}\right)\right)^{\{io\}} \tag{18}$$

$$\left(\underline{q} \cdot \underline{\xi}^{\{a,c\}}\right)^{\{a,c\}} = \left(\underline{i} \cdot \underline{\xi}^{\{a,c\}}\right)\left(E_{\{-,+\}}^{\{a,c\}} - E_{tn}^{\{a,c\}}\right) - \sum_{i \neq wv} c_{P,i} n_i^{co}\left(T - T^{\{\infty\}}\right) + \nabla \cdot \left(\hat{\lambda}\nabla T\right)^{\{sep\}} \tag{19}$$

$$\left(\underline{q} \cdot \underline{\xi}^{\{\infty\}}\right)^{\{cc\infty\}} = U\left(T - T^{\{\infty\}}\right) \tag{20}$$

In Eq. 19, E_{tn} is the thermoneutral potential, assumed to be constant. $c_{P,\mathrm{i}}$ is the specific constant-pressure heat capacity of i. The parameter U in Eq. 20 is the convective heat transfer coefficient.

2.4. Electrochemical reaction equations

Despite the significant thickness of the porous electrode, it was assumed that the reaction occurred entirely at the interface between the porous electrode and the separator. This simplifying assumption was valid for three reasons. First, in any porous electrode, the reaction always favors the separator because the magnitude of the resistance overpotential is lowest there. Second, the high capillary diffusivity led to very uniform through-plane liquid saturation profiles, so the relative electroactive area of the electrodes could be set equal to the liquid saturation at the ESI in kinetics equations. Finally, any solution resistance in the porous electrode regions was compensated by an additional area-specific resistance specified at the ESI.

The Nernst equation was used to estimate the equilibrium reduction potentials at the anode and cathode, respectively as follows:

$$E_{eq,a}^{red} = E_{eq,a}^{\circ} - \frac{RT}{F} \ln \left\{ \prod_{i=\{w,OH^-,O_2\}} a_i^{-\nu_{i,a}} \right\} \tag{21}$$

$$E_{eq,c}^{red} = E_{eq,c}^{\circ} - \frac{RT}{F} \ln \left\{ \prod_{i=\{w,OH^-,H_2\}} a_i^{\nu_{i,c}} \right\} \tag{22}$$

in which ν_i is defined as the stoichiometric coefficient of component i in the gas evolution reaction. The activities of species were calculated using Eqs. 23 through 25:

$$a_{i=\{H_2,O_2\}} = \frac{y_i P}{101325} \tag{23}$$

$$a_w = P_w / P_{w,sat}^{*} \tag{24}$$

$$a_{OH^-} = \Upsilon_{\pm,m} m_{KOH} \tag{25}$$

A stabilization procedure was applied to each ESI. The purpose was to compute local boundary resistances that would not interfere with the potential solver solution. First, an initial thermodynamic and kinetic potential drop $\Delta E_{tk}^{init\{a,c\}}$ was defined as the non-ohmic component of the total potential drop,

$$\Delta E_{tk}^{init,\{a,c\}} = E_{+}^{\{a,c\}} - E_{-}^{\{a,c\}} + \left(\underline{i} \cdot \underline{\xi}^{\{sep,c\}} \right)^{\{a,c\}} R_{esi} \tag{26}$$

for which $E_{+}^{\{a,c\}}$ and $E_{-}^{\{a,c\}}$ are extracted from the solution from the current iteration. R_{esi} is a constant value specified to account for resistance at the ESI due to gas bubbles and electrolyte resistance within the porous electrodes. To reinforce the condition $\nabla \cdot \underline{\boldsymbol{i}} = 0$, we set an apparent resistance R_{app} constant:

$$R_{app} = \frac{E_{cell} + \Delta E_{tk}^{init\{a,c\}}}{\underline{i}} \tag{27}$$

Next, activation overpotentials are defined from the potential drop as

$$\eta_{\{a,c\}} = \{+,-\}\left(-\Delta E_{tk}^{old,\{a,c\}} + E_{eq,\{a,c\}}^{red} \right) \tag{28}$$

and the overpotentials are used in the concentration dependent Tafel approximations in Eqs. 29 and 30, valid for $E_{cell} > 1.4$ V,

$$\left(\underline{i} \cdot \underline{\xi}^{\{sep\}} \right)^{\{a\}} = i_{0,\ a}^{ref} s \frac{C_{OH^-}}{4.5\ [M]} \exp\left\{ \frac{\alpha_a F \eta_a}{T} \right\} \tag{29}$$

$$\left(\underline{i} \cdot \underline{\xi}^{\{c\}} \right)^{\{c\}} = i_{0,c}^{ref} s a_w^2 \exp\left\{ \frac{-\alpha_c F \eta_c}{RT} \right\} \tag{30}$$

The above equations for current density are only guesses because while we possess a value for ΔE_{tk}, we do not yet know what the value should be. If we base R_{tk} on these guesses, we will change R_{app} and cause the condition $\nabla \cdot \underline{\boldsymbol{i}} \neq 0$, leading subsequently to run-away overcompensation and divergence of the potential solver. To find $\Delta E_{tk}^{new,\{a,c\}}$, we need to set a constraint that minimizes a residual Y; specifically, we desire the interfacial current to be equal to the current in the remainder of the cell:

$$Y = \left(\underline{i} \cdot \underline{\xi}^{\{sep,c\}} \right)^{\{a,c\}} - \frac{E_{cell} + \Delta E_{tk}^{init\{a,c\}}}{R_{app}} \tag{31}$$

So, we use a modified Newton-Raphson procedure with an under-relaxation factor of 0.9 to improve the guess for $\Delta E_{tk}^{new,\{a,c\}}$ over a number of sub-iterations until a sufficiently small Y is achieved,

$$\Delta E_{tk}^{new,\{a,c\}} = \Delta E_{tk}^{old,\{a,c\}} - 0.9 * Y / \left(\frac{\partial Y}{\partial \Delta E_{tk}^{old,\{a,c\}}} \right) \tag{32}$$

and finally calculate the stabilized R_{tk},

$$R_{tk}^{\{a,c\}} = -\frac{\Delta E_{tk}^{new,\{a,c\}}}{\left(\underline{i} \cdot \underline{\xi}^{\{sep,c\}} \right)^{\{a,c\}}} \tag{33}$$

2.5. Neutral species transport

In all fluid regions, the diffusivity of gas species i through j was a function of temperature, pressure, and liquid saturation, with reference values provided by Marrero [42],

$$\boldsymbol{D_{i-j}} = (1 - \boldsymbol{s})^{b} \boldsymbol{D_{i-j}^{ref}} \left(\frac{\boldsymbol{P_{i-j}^{ref}}}{\boldsymbol{P}} \right) \left(\frac{\boldsymbol{T}}{\boldsymbol{T_{i-j}^{ref}}} \right)^{1.75} \tag{34}$$

The phase diffusivity of the solution through the gas phase and vice versa was defined within the porous media as follows, with s^3 as the relative permeability [43]:

$$\boldsymbol{D_{L-G}^{\{por\}}} = -\frac{\boldsymbol{s}^3 \kappa}{\boldsymbol{\mu_L}} \boldsymbol{\gamma} \cos\{\boldsymbol{\theta}\} \sqrt{\epsilon/\kappa} \frac{\boldsymbol{dJ}}{\boldsymbol{ds}} \tag{35}$$

while in the manifolds, the phase diffusivity was based on the Schmidt number, which was assumed to be 100.

$$\boldsymbol{D_{L-G}^{\{man\}}} = \bar{\boldsymbol{\mu}} / (\bar{\boldsymbol{\rho}} \boldsymbol{N_{Sc}}) \tag{36}$$

Hydrogen diffusivity and solubility was obtained from Schalenbach et al. [28] Eqs. 37 and 38 were fitted to make their relationships continuous with KOH mass fraction:

$$\begin{aligned} \boldsymbol{D_{H_2-KOH}} &= 10^{-5} (\boldsymbol{K}_1 \exp\{\boldsymbol{K}_2 \boldsymbol{w_{KOH}}\} + \boldsymbol{K}_3) \\ &\quad * \exp\left\{ -\frac{(\boldsymbol{K}_4 \exp\{\boldsymbol{K}_5 \boldsymbol{w_{KOH}}\} + \boldsymbol{K}_6)}{10^{20} \boldsymbol{k_B T}} \right\} \end{aligned} \tag{37}$$

$$\begin{aligned} \boldsymbol{C_{H_2,sat}} &= 10^{-8} * \max\left\{ \boldsymbol{K}_7 \boldsymbol{w_{KOH}}^{\boldsymbol{K}_8 \boldsymbol{w_{KOH}} + \boldsymbol{K}_9}, 0.2 \right\} \\ &\quad * \exp\left\{ -\frac{\max\{\boldsymbol{K}_{10} \ln\{\boldsymbol{w_{KOH}}\} + \boldsymbol{K}_{11}, -0.51\}}{10^{20} \boldsymbol{k_B T}} \right\} \end{aligned} \tag{38}$$

The pre-exponential factors in Eqs. 37 and 38 agree to within 11% and 3%, respectively, while the activation energies agree to within 5% and 2%, respectively, at KOH weight fractions greater than 0.2. The diffusivity and solubility of oxygen in KOH solution was obtained from Tham et al. [44] and Davis et al. [45], respectively. The data from these authors was fitted using Eqs. 39 and 40:

$$\boldsymbol{D_{O_2-KOH}} = 10^{-9} \exp\left\{ \frac{\boldsymbol{K}_{12}}{\boldsymbol{T}} + \boldsymbol{K}_{13} \boldsymbol{C_{KOH}^2} + \boldsymbol{K}_{14} \boldsymbol{C_{KOH}} + \boldsymbol{K}_{15} \right\} \tag{39}$$

$$C_{O_2,sat} = 1\hat{0}\left\{ -5 + \log\left\{ K_{16} T^{K_{17}} \right\} + (K_{18} T + K_{19}) C_{KOH} \right\} \tag{40}$$

Eq. 39 is a rough fit that estimates $\ln\{D_{O_2-KOH}\}$ to within 20%. There is room for improvement, but it is beyond the scope of this work. An additional experimental study would be quite helpful in this regard. The oxygen solubility in Eq. 40 is accurate to within 2% in the temperature and concentration range of this study.

2.6. Charged species transport

If the reaction is confined to the ESI, as justified in “Electrochemical Reaction Equations,” there is a negligible change in potential within the electrode. Therefore, we neglected the mobility term in the Nernst-Planck equation. The ion diffusivity was set equal to the phase diffusivity from Eqs. 35 and 36, which was many orders of magnitude greater than the mean diffusivity of KOH in solution, allowing us to neglect the latter. Due to the transport equations being on the basis of superficial compositions, a superficial ion diffusivity was specified,

$$\boldsymbol{D^S_{KOH-L}} = \frac{\boldsymbol{D_{L-G}}}{\boldsymbol{s}}\left(1 - \frac{\boldsymbol{C_{KOH}}\|\nabla \boldsymbol{s}\|}{\|\nabla \boldsymbol{C^S_{KOH}}\|}\right) \tag{41}$$

which is valid when ∇s and ∇C^S_{KOH} point in the same direction. This is assumed to be the case because C^S_{KOH} is defined as sC_{KOH} and is therefore proportional to s.

Charged species transport in the separator was neglected in this work because we are not yet sure if it is necessary to model a change in concentration under the set operating conditions. The charged species transport model will be used to determine if there are appreciable changes in KOH concentration within the electrodes and PTLs before considering a separator transport model.

2.7. CFD solution method

Siemens Simcenter Star-CCM+ 2020.1.1 Build 15.02.009 was used to solve the governing equations using the finite volume method. The SIMPLE algorithm was applied with Gauss-Seidel relaxation. Conjugate gradient acceleration was applied to the pressure solver. Final under-relaxation factors of 0.7, 0.3, 0.995, 0.995, 0.995, 0.9995, and 1.0 were set for the velocity, pressure, neutral species, charged species, fluid energy, solid energy, and potential solvers, respectively. A flow solution with no reaction was obtained prior to initiating the other solvers. The potential solver was activated second, with the solution occurring in four stages:

1) A 0-dimensional (0D) model was used to determine constant values of interfacial resistance, including R_{esi} and R_{tk}, at the anode and cathode, which were used for tens of iterations.
2) The Newton-Raphson-stabilized electrochemical reaction model described in “Electrochemical Reaction Equations” was allowed to compute new local values for interfacial resistance.
3) The charged species solver was ramped from 0 over 100 iterations to solve for the concentration of KOH in the channels, PTLs, and electrodes.
4) At the end of the charged species solver ramp, the neutral species and energy solvers were ramped from 0 over 300 iterations. Compressibility, gas and solution crossover, and gas diffusion limitations due to the presence of the liquid phase were not considered until well after a stable solution was obtained. Thereafter, convergence was said to be achieved after the residuals stabilized and the current density varied by less than 10 A m^{-2} in 1000 iterations at a slowing rate.

Simulations were conducted with several sets of operating conditions, which are listed in Table 4.

Table 4
Operating Conditions

Series	Case	Cell Potential (V)	Anode Feed Rate (L min^{-1})	Cathode Feed Rate (L min^{-1})
A	1	1.6	8.107	8.107
	2	1.8	8.107	8.107
	3	2.0	8.107	8.107
	4	2.2	8.107	8.107
	5	2.4	8.107	8.107
B	1	2.4	2.027	2.027

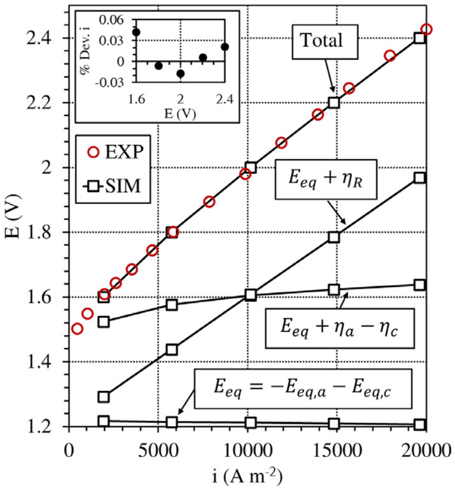

Fig. 3. Comparison of polarization curves collected during experiments and simulations under Series A operating conditions. The simulated polarization curve is decomposed to show the potential components. The insert shows a relative error in current density not exceeding 5%.

3. Results and discussion

3.1. Cell performance

The validation of simulated performance is provided in the polarization curves in Fig. 3. The deviations in model current density from experimental values were no more than 5% from 1.6 to 2.4 V at 80°C with 1 atm balanced pressure setpoints and a solution feed rate of 11.1 mL min^{-1} cm^{-2} to each the anode and cathode. Current distributions are shown in Fig. 4a. The absolute nonuniformity of these distributions increases with increasing current density as expected. Current density is lowest in the region near the anode inlet and cathode outlet. This is well explained by Fig. 4b, which indicates that the highest gas volume fraction of up to 0.6 is located in this region. The presence of the gas phase impacts electrode kinetics by preventing the utilization of all active sites. The gas volume fraction is highest near the cathode outlet – as opposed to the anode outlet – because of the reaction stoichiometry, which leads to twice as many moles of hydrogen as moles of oxygen.

3.2. Local solution properties

The concentration of the KOH solution is an important variable, given its role in calculating exchange current density and conductivity. In these simulations, as explained previously, we wished to maintain a constant value for solution concentration in the separator and, via this work, determine whether a detailed ion transport model is required for the separator. Additionally, we set a constant value for the ESI resistance. Therefore, the local concentration was

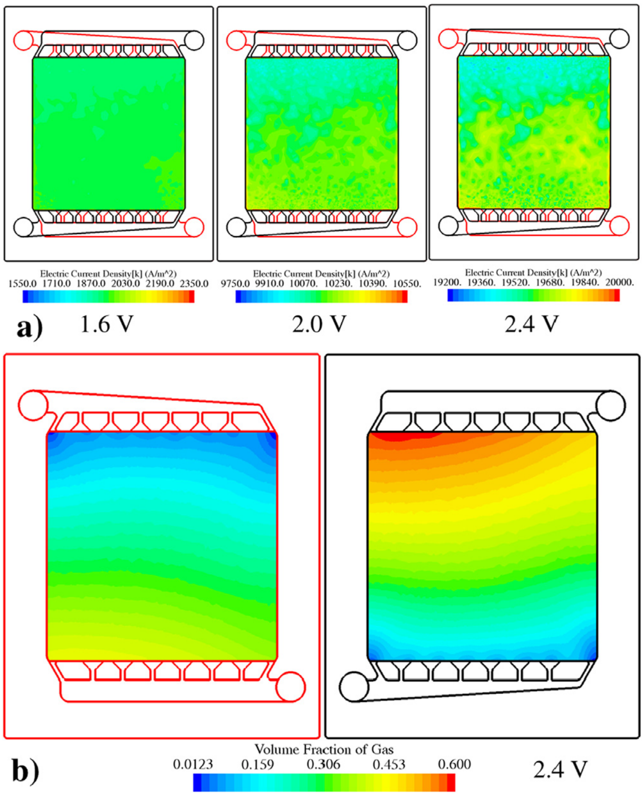

Fig. 4. a) Current density distributions for Series A operating conditions. The color bar scales are the same size at different magnitudes so that the increase in non-uniformity can be observed with an increase in cell potential. b) Gas volume fraction distributions at the anodic ESI (left) and the cathodic ESI (right) for Case A-5.

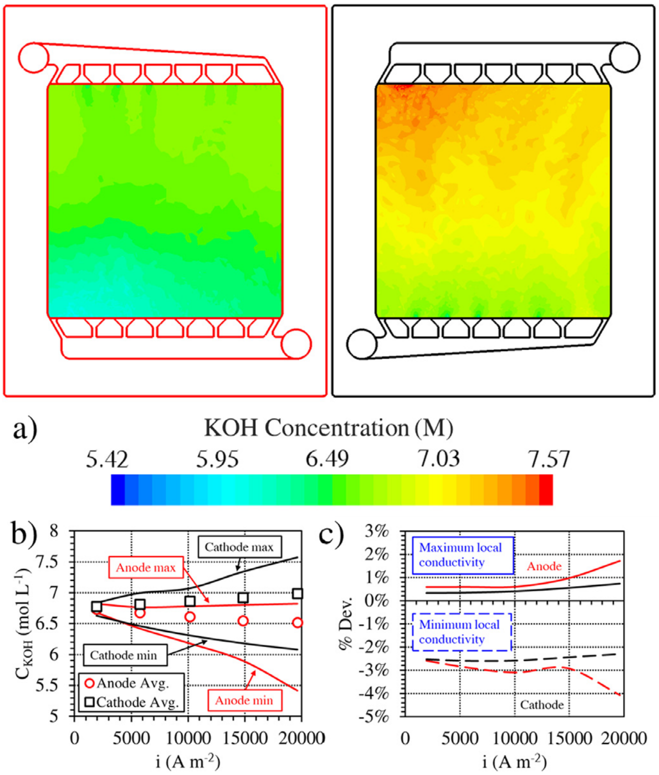

Fig. 5. a) The KOH concentration distribution at the anodic ESI (left) and the cathodic ESI (right) for Case A-5. b) Effect of current density on the minimum, maximum, and average KOH concentrations in the anodic and cathodic electrode and PTL regions. The average KOH concentrations are represented by the hollow points. c) The maximum and minimum percent deviations of conductivity in the electrodes and PTLs from the conductivity of the separator. The separator conductivity was a function only of temperature because its KOH concentration was fixed.

assumed not to impact cell performance. However, the concentration distributions were studied in order to motivate further study of ion transport.

Fig. 5a presents the KOH concentration distributions at the anode and cathode. Even at a considerably high flow rate of 8.107 L min^{-1} per half-cell, there is a significant variation in local KOH concentration. At the anode, the concentration decreases from inlet to outlet as water is produced in the OER. At the cathode, concentration increases from inlet to outlet as water is consumed in the HER. Due to the countercurrent configuration, this results in low KOH concentration on both sides of the separator near the anode outlet and cathode inlet. Consequently, the separator concentration should also decrease from the inlet concentration in this region, which would increase the cell resistance. Fig. 5b plots the average, minimum, and maximum KOH concentrations in the electrode and PTL regions versus average current density for Series A. Generally, the cathode concentration is higher than that of the anode, which is due to water production at the anode and water consumption at the cathode. According to the graph, if we modeled ion transport in the separator, KOH would generally diffuse from the cathode to the anode. However, a higher concentration of KOH at the cathode would not necessarily lead to net flux toward the anode if the solution undergoes convection from the anode to the cathode. This phenomenon has been experimentally observed by others [18,29] and is predicted by our model to happen locally in our geometry, especially at low current density. More on solution transport will be discussed in a later section. Fig. 5c shows that the deviation of the local solution conductivity from the average separator conductivity can be as high as 4% under Series A operating conditions. The concentration distributions rationalize the development of a separator transport model and an ESI model for 3D simulations.

Changes in concentration of the magnitudes computed in the model could impact fluid flow. The liquid viscosity at the cathode varied from 8.2e-4 Pa s at the cell inlet to about 1e-3 Pa s in the area with the highest concentration. This may have played a minor role in exacerbating the issue of low local current density in the region with high gas volume fraction by increasing the resistance to flow.

3.3. Undesired crossover of gases

In this work, hydrogen and oxygen gases were assumed to travel through the separator via two mechanisms: diffusion and convection of dissolved species. Bubbling was not considered due to total pressures being below the bubble point of the Zirfon® separator. Therefore, the local flux of gases depended strongly on the direction of solution flow. Solution transport was governed by liquid pressure drop and electroosmotic drag, which could either be cooperating or competing factors. The liquid pressure was dependent on two factors – the liquid saturation and the feed rate – while electroosmotic drag depended only on current density.

Fig. 6 shows how the direction of solution flow across the separator is affected by operating conditions. Consider Case A-1 operating conditions. The pressure drop from inlet to outlet was high and the current density was very low. Consequently, capillary action and electroosmotic drag contributed minimally to transport. The DLP was influenced primarily by the pressure drops from inlet to outlet as a result of the high solution feed rate. The solution

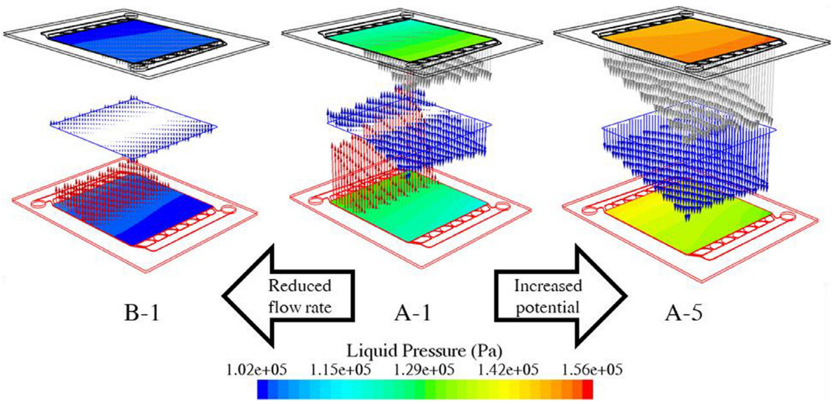

Fig. 6. Anodic and cathodic liquid pressure distributions and flux vectors representing the flow of electrolyte and dissolved gases through the separator in Cases A-1, A-5, and B-1. The anode is outlined in red while the cathode is outlined in black. In the liquid pressure distributions, red indicates high liquid pressure while blue indicates low liquid pressure. Gray, blue, and red vectors indicate fluxes of hydrogen, electrolyte, and oxygen, respectively.

travelled in the +z direction near the anode inlet and the -z direction near the cathode inlet. For Case A-5, the high gas evolution rate resulted in higher pressure drops. Again, capillary action was a miniscule factor of DLP compared to pressure drops. Liquid pressure was always higher in the cathode than in the anode despite higher liquid saturations existing in the anode. This was due to the higher volume of gas production in the cathode, the effects of which are more prominent at high current densities. Additionally, electroosmotic drag of water from cathode to anode was a greater factor than in Case A-1. Ultimately, solution travelled only in the -z direction. For Case B-1, the pressure drops decreased in both sides of the cell due to the lower feed rate, so the magnitude of the DLP decreased significantly. So, while pressure drop was still the dominating factor, DLP became more sensitive to liquid saturation than in Case A-1. Unlike Case A-1, there is no obvious bias in solution flow from cathode to anode in Case B-1.

It is important to note that osmosis was not considered for water transport. The variations in concentration suggested by the model indicate that osmosis is a possible factor. This would promote additional liquid water flux from anode to cathode. This provides further rationale for us to include an ion transport model for the separator in future work.

Fig. 6 also shows the effect of solution transport on gas crossover. Gas generally travelled in the same direction as the solution unless the solution velocity was very low. In Case A-5, oxygen crossover was completely suppressed due to the strong convection of solution from cathode to anode at all locations. At low solution velocity, diffusion flux could dominate over opposing convection flux. Note that oxygen crossover in Case B-1 occurs over a larger area, with diffusion being the more prominent transport mechanism in relatively stagnant solution in the middle of the cell. At all cell potentials and flow rates, oxygen crossover was more prominent if the solution moved in the +z direction, while hydrogen crossover was more prominent if the solution moved in the -z direction. In light of this, gas crossover was moderated by limiting convective transport through the separator, as seen when comparing Cases A-1 and B-1.

Two measures of the extent of gas crossover, the percent of the lower flammability limit (%LFL) at the anode and percent hydrogen purity at the cathode, are presented in Fig. 7. The %LFL was calculated from the dry gas composition using a lower flammability limit of 4% H_2 in O_2. The percent hydrogen purity (%H_2P) at the cathode was also calculated on a dry basis. The exponential decrease in %LFL with increasing current density is due to the increase in gas production, which dilutes crossover products. The

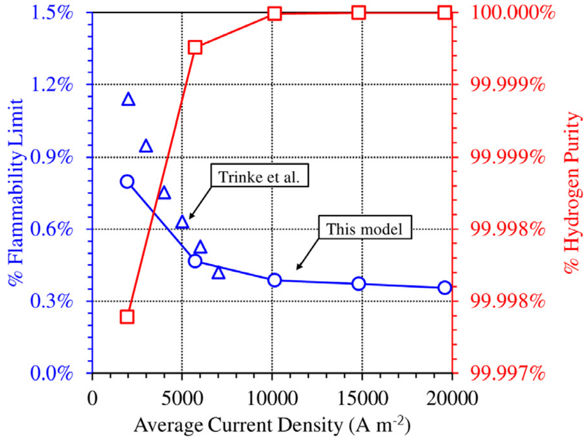

Fig. 7. The response in the percent flammability limit at the anode outlet and the percent hydrogen purity at the cathode outlet for Series A. Percentages are based on volume. The data points (approximate) from Trinke et al. [11] are overlayed for comparison, corresponding to operation with unmixed electrolyte feed, which was consistent with simulation inlet conditions.

%H_2P increases with increasing current density for the same reason. As a measure of sanity, values of %LFL were compared to those presented by Trinke et al. [11] for ADWE devices with unmixed feed solution. Their experimental data were consistent with our simulations, which assumed that the feed was a fixed concentration and contained no mixtures of dissolved gases.

3.4. Demonstrations of diagnostics

The major advantage of 3D modeling is that local variations in variables, some of which may be undesired, can be linked to an aspect of the design. In Fig. 8a, we diagnose the reduction in current density near the cathode outlet. Earlier, we attributed this to the high volume fraction of hydrogen gas in that region. This is referred to as the “direct cause” in Fig. 8a. The pressure distribution and in-plane velocity vectors allow us to examine the “root cause” of the high void fraction. There is clearly a path of least resistance within which fluid flows toward the outlet, causing an asymmetric velocity profile. The low fluid velocity in the problem region is allowing higher void fractions. This can be resolved by changing the geometry of the outlet manifolds, possibly by restricting channels closer to the outlet and expanding channels far from the outlet.

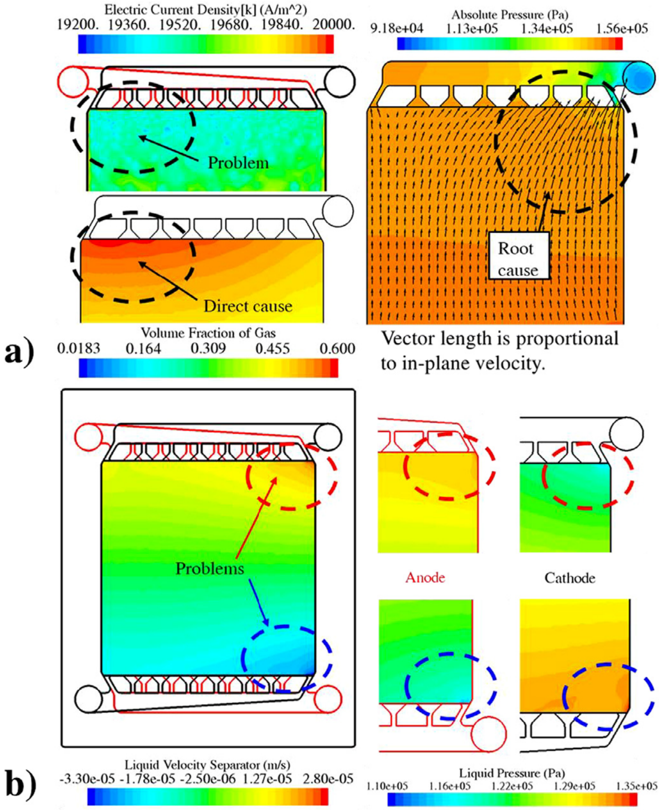

Fig. 8. a) Diagnostic analysis of a problem area with low current density due to high gas volume fraction. The root cause was determined to be associated with the flow distribution, which led to stagnation of flow within the problem area. b) Diagnostic analysis of geometric features leading to increased electrolyte velocity, i.e., local crossover, in the designated problem areas. The problem areas are color-coded for ease of correlation. Liquid pressure differentials, shown on the right, were found to exist at extrema in the problem areas.

Bear in mind that adding a turbulence model may affect the computed flow distribution by increasing the local effective viscosity in regions of the manifolds with high fluid velocities.

We can also see geometry effects on local crossover. Fig. 8b illustrates a diagnostics procedure similar to that in Fig. 8a. Problem areas, i.e., areas with high liquid velocity magnitudes leading to high gas crossover, are identified. Then, the local liquid pressure distributions are plotted to show that the DLP across the separator was at extremes in these problem areas. The problem areas arise when inlet and outlet manifold channels overlap, leading to large differences in liquid saturation across the separator. This can be resolved by ensuring that there are no overlaps if possible. Of course, if gas crossover were insignificant, there would be no need to make corrective actions.

4. Conclusion

We employed a 3D CFD model to examine liquid saturation, concentration, and crossover distributions under different operating conditions. Local reductions in current density were linked to high void fractions, primarily that of the cathode. We found that these high void fractions were attributed to aspects of the geometry and that the channel design can be altered to prevent those conditions. In the absence of an ion transport model for the separator, the results suggested that solution concentrations may vary significantly above and below the inlet concentration. This finding motivates the implementation of a separator transport model. The need to specify resistances at the anodic and cathodic ESI motivates the modeling of these interfaces. Simulated crossover of hydrogen, oxygen, and the solution was investigated. Overall crossover was strongly linked to solution feed rate and cell potential, and local crossover near the inlets and outlets was attributed to the overlapping of the injection and ejection channels. Simulations such as this one can be utilized to design major components of next-generation ADWE devices to maximize their efficiency at the desired hydrogen production rate.

Nomenclature

Latin

Symbol	Variable	Unit
A	Cross-sectional area	
a	Activity	None
b	Bruggeman exponent	None
C	Molar concentration	M
c_P	Constant pressure heat capacity	J kg^{-1} K^{-1}
D	Diffusivity	m^2 s^{-1}
E	Potential	V
F	Faraday constant	C kmol^{-1}
h	Specific enthalpy	J kg^{-1}
$\underline{I}$	Identity matrix	None
$\underline{\boldsymbol{i}}$	Current density	A m^{-2}
i_0	Exchange current density	A m^{-2}
J	Leverett function	None
K_j	Parameter j	variable
k	Relative permeability	none
k_B	Boltzmann constant	J K^{-1}
L	Through-plane length	M
M	Molecular weight	kg kmol^{-1}
S	Volumetric source term	kg m^{-3} s^{-1}
s	Liquid saturation	none
T	Temperature	K
U	Convective heat transfer coefficient	W m^{-2} K^{-1}
$\underline{\boldsymbol{v}}$	Velocity	m s^{-1}
w	Mass fraction	none
x	Mole fraction in liquid phase	none
Y	Residual current density	A m^{-2}
y	Mole fraction in gas phase	none

Greek

Symbol	Variable	Unit
α	Transfer coefficient	none
γ	Surface tension	N m^{-1}
ϵ	Porosity	none
η	Overpotential	V
θ	Wetting angle	rad
κ	Intrinsic permeability	m^2

(continued on next page)

(*continued*)

m	Molal concentration	mol kg^{-1}	λ	Thermal conductivity	W m^{-1} K^{-1}
N_{Sc}	Schmidt number	none	μ	Dynamic viscosity	Pa s
n	Boundary normal mass flux	kg m^{-2} s^{-1}	ν	Stoichiometric coefficient	mol (mol e$^-$)$^{-1}$
n_d	Electroosmotic drag coefficient	mol (mol OH$^-$)$^{-1}$	$\underline{\boldsymbol{\xi}}$	Inner normal unit vector	none
P	Pressure	Pa	ρ	Density	kg m^{-3}
Q	Volumetric flow rate	L min^{-1}	σ	Conductivity	S m^{-1}
$\underline{\boldsymbol{q}}$	Heat flux	W m^{-2}	$\underline{\underline{T}}$	Viscous stress tensor	kg m^{-1} s^{-1}
R	Resistance	Ω m^2	τ	Tortuosity	none
$\mathcal{R}$	Universal gas constant	J kmol^{-1} K^{-1}	$\Upsilon_{\pm,m}$	Molal activity coefficient	none
$\underline{\underline{R}}$	Viscous resistance	Pa s m^{-2}			
Subscripts					
Symbol	Description	Symbol	Description	Symbol	Description
a	Anodic	wv	Water vapor	$\{cc\infty\}$	See Table 1
app	Apparent	Ω	Ohmic	$\{ima\}$	See Table 1
c	Cathodic	$+$	At the +z side of the boundary	$\{imc\}$	See Table 1
cap	Capillary	$-$	At the -z side of the boundary	$\{ina\}$	See Table 1
$cell$	Across or of the cell			$\{inc\}$	See Table 1
e	Of energy	Superscripts		$\{io\}$	See Table 1
e^-	Electron	Symbol	Description	$\{man\}$	See Table 1
eff	Effective	co	Due to crossover	$\{outa\}$	See Table 1
eq	At equilibrium	$init$	Initial guess or condition	$\{outc\}$	See Table 1
esi	Of the effective gap	new	Value for next sub-iteration	$\{por\}$	See Table 1
G	Gas phase	old	Value from current sub-iteration	$\{sep\}$	See Table 1
H_2	Hydrogen	red	Reduction reaction	$\{f\}$	See Table 1
i	Of Species i	ref	At the reference state	$\{+\}$	See Table 1
$i-j$	Of i moving through j	rxn	Due to reaction	$\{-\}$	See Table 1
KOH	Potassium hydroxide	S	Superficial	$\{\infty\}$	Environment
L	Liquid phase	vap	Of vaporization		
O_2	Oxygen	$*$	Pure component	Other	
OH^-	Hydroxide anion	$\circ$	At standard state	Symbol	Description
sat	At water vapor saturation	$\{a\}$	See Table 1	Π	Phase
tk	Thermodynamic and kinetic	$\{c\}$	See Table 1	$\bar{\varphi}$	Volume- average phi
tn	Thermoneutral	$\{ccma\}$	See Table 1	$\hat{\varphi}$	Mass- average phi
w	Water	$\{ccmc\}$	See Table 1	$\breve{\varphi}$	Mole- average phi

Declaration of Competing Interest

The authors have no conflicts of interest to declare.

Acknowledgements

This work was funded in part by the University of South Carolina Hydrogen and Fuel Cell Center. Additional financial support was received from the Gwangju Institute of Science and Technology (GIST) and Korea Institute of Energy Research (KIER). This research was supported by the Hydrogen Energy Innovation Technology Development Program of the National Research Foundation (NRF) of Korea funded by the Ministry of Science and ICT (NRF-2019M3E6A10644287).

Star-CCM+ 15.02.009-R8 was provided by Siemens Product Lifecycle Management Software Inc. The CAD geometry of the cell was prepared using SolidWorks 2018, provided by Dassault Systèmes® SE.

Appendix A

Derivation of Superficial Diffusivity

Diffusional transport of species in a continuum containing two phases is assumed to be governed by Fick's Law:

$$\underline{\boldsymbol{n}}^S_{diff} = -D^S \nabla C^S \tag{A.1}$$

The superscript S indicates that the solute is assumed to be dissolved in every species within the continuum. This assumption is invalid for a continuum containing two or more phases, so we are interested in applying the below equation:

$$\underline{\boldsymbol{n}}_{diff} = -D \nabla C \tag{A.2}$$

However, the pseudo-two-phase assumption is employed in the model. To obtain the desired species flux, we must use the desired diffusivity D to calculate a superficial diffusivity D_S such that $\underline{\boldsymbol{n}}_{diff} = \underline{\boldsymbol{n}}^S_{diff}$. The definition of the concentration C is as follows:

$$C = \frac{C^S}{s} \tag{A.3}$$

in which s is the volume fraction of the solution phase through which the species of interest is transported. Substituting Equation A.3 into Equation A.2, applying the quotient rule, and setting $\underline{\boldsymbol{n}}_{diff} = \underline{\boldsymbol{n}}^S_{diff}$, we obtain

$$D^S \nabla C^S = D\left(\frac{1}{s}\nabla C^S - \frac{C^S}{s^2}\nabla s\right) \tag{A.4}$$

Upon simplification, assuming that ∇C^S is co-parallel to ∇s, we get the input diffusivity D^S as a function of the desired diffusivity D:

$$D^S = \frac{D}{s}\left(1 - \frac{C\|\nabla s\|}{\|\nabla C^S\|}\right) \tag{A.5}$$

References

[1] RK Pachauri, Mayer Leo, Intergovernmental panel on climate change, Clim. Change (2014) synthesis report. n.d..

[2] M Felgenhauer, T. Hamacher, State-of-the-art of commercial electrolyzers and on-site hydrogen generation for logistic vehicles in South Carolina, Int. J. Hydrogen Energy 40 (2015) 2084–2090, doi:10.1016/j.ijhydene.2014.12.043.

[3] A Ursúa, LM Gandía, P. Sanchis, Hydrogen production from water electrolysis: current status and future trends, in: Proceedings of the IEEE, 100, Institute of Electrical and Electronics Engineers Inc., 2012, pp. 410–426, doi:10.1109/JPROC.2011.2156750.

[4] M Schalenbach, G Tjarks, M Carmo, W Lueke, M Mueller, D. Stolten, Acidic or alkaline? towards a new perspective on the efficiency of water electrolysis, J. Electrochem. Soc. 163 (2016) F3197–F3208, doi:10.1149/2.0271611jes.

[5] A Manabe, H Domon, J Kosaka, T Hashimoto, T Okajima, T. Ohsaka, Study on separator for alkaline water electrolysis, J. Electrochem. Soc. 163 (2016) F3139–F3145, doi:10.1149/2.0191611jes.

[6] DM See, RE. White, Temperature and concentration dependence of the specific conductivity of concentrated solutions of potassium hydroxide, J. Chem. Eng. Data 42 (1997) 1266–1268.

[7] H. Vogt, The actual current density of gas-evolving electrodes - notes on the bubble coverage, Electrochim. Acta 78 (2012) 183–187, doi:10.1016/j.electacta.2012.05.124.

[8] MT de Groot, AW. Vreman, Ohmic resistance in zero gap alkaline electrolysis with a Zirfon diaphragm, Electrochim. Acta 369 (2021) 137684, doi:10.1016/j.electacta.2020.137684.

[9] C González-Buch, I Herraiz-Cardona, E Ortega, J García-Antón, V. Pérez-Herranz, Synthesis and characterization of macroporous Ni, Co and Ni-Co electrocatalytic deposits for hydrogen evolution reaction in alkaline media, Int. J. Hydrogen Energy 38 (2013) 10157–10169, doi:10.1016/j.ijhydene.2013.06.016.

[10] P Ganesan, A Sivanantham, S. Shanmugam, Inexpensive electrochemical synthesis of nickel iron sulphides on nickel foam: super active and ultra-durable electrocatalysts for alkaline electrolyte membrane water electrolysis, J. Mater. Chem. A 4 (2016) 16394–16402, doi:10.1039/c6ta04499a.

[11] P Trinke, P Haug, J Brauns, B Bensmann, R Hanke-Rauschenbach, T. Turek, Hydrogen crossover in PEM and alkaline water electrolysis: mechanisms, direct comparison and mitigation strategies, J. Electrochem. Soc. 165 (2018) F502–F513, doi:10.1149/2.0541807jes.

[12] In Lee H, DT Dung, J Kim, JH Pak, Kim S kyung, HS Cho, et al., The synthesis of a Zirfon-type porous separator with reduced gas crossover for alkaline electrolyzer, Int. J. Energy Res. 44 (2020) 1875–1885, doi:10.1002/er.5038.

[13] HI Lee, M Mehdi, SK Kim, HS Cho, MJ Kim, WC Cho, et al., Advanced Zirfon-type porous separator for a high-rate alkaline electrolyser operating in a dynamic mode, J. Membr. Sci. 616 (2020) 118541, doi:10.1016/j.memsci.2020.118541.

[14] C-Y Hung, S-D Li, C-C Wang, C-Y. Chen, Influences of a bipolar membrane and an ultrasonic field on alkaline water electrolysis, J. Membr. Sci. 389 (2012) 197–204, doi:10.1016/j.memsci.2011.10.050.

[15] N Nagai, M Takeuchi, T Kimura, T. Oka, Existence of optimum space between electrodes on hydrogen production by water electrolysis, Int. J. Hydrogen Energy 28 (2003) 35–41.

[16] R Phillips, CW. Dunnill, Zero gap alkaline electrolysis cell design for renewable energy storage as hydrogen gas, RSC Adv. 6 (2016) 100643–100651, doi:10.1039/c6ra22242k.

[17] J Rodríguez, S Palmas, M Sánchez-Molina, E Amores, L Mais, R. Campana, Simple and precise approach for determination of Ohmic contribution of diaphragms in alkaline water electrolysis, Membranes 9 (2019), doi:10.3390/membranes9100129.

[18] JW. Haverkort, Modeling and experiments of binary electrolytes in the presence of diffusion, migration, and electro-osmotic flow, Phys. Rev. Appl. 14 (2020) 044047, doi:10.1103/PhysRevApplied.14.044047.

[19] V Kienzlen, D Haaf, W. Schnurnberger, Location of hydrogen gas evolution on perforated plate electrodes in zero gap cells, Int. J. Hydrogen Energy 19 (1994) 729–732.

[20] J Lopata, Z Kang, J Young, G Bender, JW Weidner, S. Shimpalee, Effects of the transport/catalyst layer interface and catalyst loading on mass and charge transport phenomena in polymer electrolyte membrane water electrolysis devices, J. Electrochem. Soc. 167 (2020) 064507, doi:10.1149/1945-7111/ab7f87.

[21] Leverett MC. Capillary behavior in porous solids. American Institute of Mining Engineers, 1940, p. 152–69.

[22] WA Moseley, VK. Dhir, Capillary pressure-saturation relations in porous media including the effect of wettability, J. Hydrol. 178 (1996) 33–53.

[23] JT Gostick, MW Fowler, MA Ioannidis, MD Pritzker, YM Volfkovich, A. Sakars, Capillary pressure and hydrophilic porosity in gas diffusion layers for polymer electrolyte fuel cells, J. Power Sources 156 (2006) 375–387, doi:10.1016/j.jpowsour.2005.05.086.

[24] EC Kumbur, Sharp K v., MM Mench, On the effectiveness of Leverett approach for describing the water transport in fuel cell diffusion media, J. Power Sources 168 (2007) 356–358, doi:10.1016/j.jpowsour.2007.02.054.

[25] ZH Wang, CY Wang, KS. Chen, Two-phase flow and transport in the air cathode of proton exchange membrane fuel cells, J. Power Sources 94 (2001) 40–50.

[26] C-Y Wang, C. Beckermann, A two-phase mixture model of liquid-gas flow and heat transfer in capillary porous media-I. Formulation, Int. J. Heat Mass Transfer 36 (1993) 2747–2758.

[27] DR Dekel, IG Rasin, M Page, S. Brandon, Steady state and transient simulation of anion exchange membrane fuel cells, J. Power Sources 375 (2018) 191–204, doi:10.1016/j.jpowsour.2017.07.012.

[28] M Schalenbach, W Lueke, D. Stolten, Hydrogen diffusivity and electrolyte permeability of the zirfon PERL separator for alkaline water electrolysis, J. Electrochem. Soc. 163 (2016) F1480–F1488, doi:10.1149/2.1251613jes.

[29] JW Haverkort, H. Rajaei, Electro-osmotic flow and the limiting current in alkaline water electrolysis, J. Power Sources Adv. 6 (2020) 100034, doi:10.1016/j.powera.2020.100034.

[30] LC Jacobson, X Ren, V. Molinero, Assessing the effects of crowding, pore size, and interactions on electro-osmotic drag coefficients, J. Phys. Chem. C 118 (2014) 2093–2103, doi:10.1021/jp410910r.

[31] MD Mat, K Aldas, OJ. Ilegbusi, A two-phase flow model for hydrogen evolution in an electrochemical cell, Int. J. Hydrogen Energy 29 (2004) 1015–1023, doi:10.1016/j.ijhydene.2003.11.007.

[32] H Riegel, J Mitrovic, K. Stephan, Role of mass transfer on hydrogen evolution in aqueous media, J. Appl. Electrochem. 28 (1998) 10–17.

[33] AC Olesen, C Rømer, SK. Kær, A numerical study of the gas-liquid, two-phase flow maldistribution in the anode of a high pressure PEM water electrolysis cell, Int. J. Hydrogen Energy 41 (2016) 52–68, doi:10.1016/j.ijhydene.2015.09.140.

[34] SS Lafmejani, AC Olesen, SK. Kær, VOF modelling of gas–liquid flow in PEM water electrolysis cell micro-channels, Int. J. Hydrogen Energy 42 (2017) 16333–16344, doi:10.1016/j.ijhydene.2017.05.079.

[35] D Le Bideau, P Mandin, M Benbouzid, M Kim, M Sellier, F Ganci, et al., Eulerian two-fluid model of alkaline water electrolysis for hydrogen production, Energies 13 (2020) 3394, doi:10.3390/en13133394.

[36] J Nie, Y. Chen, Numerical modeling of three-dimensional two-phase gas-liquid flow in the flow field plate of a PEM electrolysis cell, Int. J. Hydrogen Energy 35 (2010) 3183–3197, doi:10.1016/j.ijhydene.2010.01.050.

[37] K Aldas, N Pehlivanoglu, MD. Mat, Numerical and experimental investigation of two-phase flow in an electrochemical cell, Int. J. Hydrogen Energy 33 (2008) 3668–3675, doi:10.1016/j.ijhydene.2008.04.047.

[38] WA El-Askary, IM Sakr, KA Ibrahim, A. Balabel, Hydrodynamics characteristics of hydrogen evolution process through electrolysis: numerical and experimental studies, Energy 90 (2015) 722–737, doi:10.1016/j.energy.2015.07.108.

[39] M Upadhyay, S Lee, S Jung, Y Choi, S Moon, H. Lim, Systematic assessment of the anode flow field hydrodynamics in a new circular PEM water electrolyser, Int. J. Hydrogen Energy 45 (2020) 20765–20775, doi:10.1016/j.ijhydene.2020.05.164.

[40] J Rodríguez, E. Amores, CFD modeling and experimental validation of an alkaline water electrolysis cell for hydrogen production, Processes 8 (2020) 1634, doi:10.3390/pr8121634.

[41] G Zhou, Chen L der, JP Seaba, Effects of property variation and ideal solution assumption on the calculation of the limiting current density condition of alkaline fuel cells, J. Power Sources 196 (2011) 4923–4933, doi:10.1016/j.jpowsour.2011.02.026.

[42] TR. Marrero, A Comprehensive Critical Evaluation of Experimental Studies and Correlations of Results, 1970.

[43] Q Ye, T van Nguyen, Three-dimensional simulation of liquid water distribution in a PEMFC with experimentally measured capillary functions, J. Electrochem. Soc. 154 (2007) B1242–B1251, doi:10.1149/1.2783775.

[44] MK Tham, RD Walker, KE. Gubbins, Diffusion of oxygen and hydrogen in aqueous potassium hydroxide solutions, J. Phys. Chem. 74 (1970) 1747–1751.

[45] RE Davis, GL Horvath, CW. Tobias, The solubility and diffusion coefficient of oxygen in potassium hydroxide solutions, Electrochim. Acta 12 (1967) 287–297, doi:10.1016/0013-4686(67)80007-0.

[46] M Hammoudi, C Henao, K Agbossou, Y Dubé, ML. Doumbia, New multi-physics approach for modelling and design of alkaline electrolyzers, Int. J. Hydrogen Energy 37 (2012) 13895–13913, doi:10.1016/j.ijhydene.2012.07.015.

[47] Chemical Rubber Company (CRC)CRC Handbook of Chemistry and Physics, 65th ed., CRC Press, Inc., Boca Raton, Florida, U.S.A., 1984.

[48] Crane Company, Flow of Fluids Through Valves, Fittings, and Pipe, 25th ed., Technical Paper No. 410 (TP 410), 1988.

[49] RM Felder, RW. Rousseau, Elementary Principles of Chemical Processes, 3rd ed., John Wiley & Sons, Inc., Hoboken, NJ, 2005.

[50] D Le Bideau, P Mandin, M Benbouzid, M Kim, M Sellier, Review of necessary thermophysical properties and their sensivities with temperature and electrolyte mass fractions for alkaline water electrolysis multiphysics modelling, Int. J. Hydrogen Energy 44 (2019) 4553–4569, doi:10.1016/j.ijhydene.2018.12.222.

[51] Chemical Rubber Company (CRC)Aqueous Solutions of Electrolytes, CRC Press, Inc., Boca Raton, FL, U.S.A., 1992.

[52] MF Kibria, MS. Mridha, Electrochemical studies of the nickel electrode for the oxygen evolution reaction, Int. J. Hydrogen Energy 21 (1996) 179–182.

[53] I Herraiz-Cardona, C González-Buch, C Valero-Vidal, E Ortega, V. Pérez-Herranz, Co-modification of Ni-based type Raney electrodeposits for hydrogen evolution reaction in alkaline media, J. Power Sources 240 (2013) 698–704, doi:10.1016/j.jpowsour.2013.05.041.

[54] P Novotný, O. Söhnel, Densities of binary aqueous solutions of 306 inorganic substances, J. Chem. Eng. Data 33 (1988) 49–55.

[55] Z Li, KS. Pitzer, Thermodynamics of aqueous KOH over the full range to saturation and to 573 K, J. Solution Chem. 25 (1996) 813–821.

[56] PM Dunlap, SM. Faris, Surface tension of aqueous solutions of potassium hydroxide, Nature 196 (1962) 1312–1313.

[57] ML Huber, AH. Harvey, Thermal conductivity of gases, CRC Handbook of Chemistry and Physics, 92nd ed., CRC Press, Inc., Boca Raton, FL, U.S.A., 2011.

[58] EW Lemmon, MO McLinden, DG. Friend, Thermophysical properties of fluid systems, in: NIST Chemistry WebBook, NIST Standard Reference Database Number 69, National Institute of Standards and Technology, Gaithersburg, MD, 2017, p. 20899.